INL/JOU-23-71194-Revision-0

Measurements of the Thermal Conductivity of Reference Liquids Using a Modified Transient Hot-wire Needle Probe

June 2022

Brian Merritt, Troy Munro, Kurt L Davis

Changing the World's Energy Future

Idaho National Laboratory

INL is a U.S. Department of Energy National Laboratory operated by Battelle Energy Alliance, LLC

INL/JOU-23-71194-Revision-0

Measurements of the Thermal Conductivity of Reference Liquids Using a Modified Transient Hot-wire Needle Probe

Brian Merritt, Troy Munro, Kurt L Davis

June 2022

Idaho National Laboratory
Idaho Falls, Idaho 83415

http://www.inl.gov

Prepared for the
U.S. Department of Energy
Under DOE Idaho Operations Office
Contract DE-AC07-05ID14517

Measurements of the Thermal Conductivity of Reference Liquids Using a Modified Transient Hot-wire Needle Probe

B. Merritt,[1] M. Seneca,[1] S. Larson,[1] K. Davis,[2] and T. Munro*[1]
[1)] *Brigham Young University, Dept. of Mechanical Engineering, Provo, UT, USA*
[2)] *Idaho National Laboratory, High Temperature and Test Lab, Idaho Falls, ID, USA*

(*Electronic mail: troy.munro@byu.edu)

(Dated: 9 February 2023)

Many power generation processes feature some type of working fluid that plays a critical role in the transfer of heat throughout the system. To optimize thermal efficiencies, an accurate characterization of the temperature-dependent thermal conductivity of the fluid is needed. This study develops a time-domain Modified Transient Hot-wire Needle Probe to overcome phenomena that have impaired traditional measurement techniques when the fluid is both corrosive and at an elevated temperature. First, the physical design of the instrument is presented to demonstrate features that limit interference from corrosion, electrical conduction, and convective and radiative heat transfer. Next, a governing equation for 1D (radial) heat conduction is fully developed using the thermal quadrupoles technique. A finite-element study is performed for validation. A sensitivity analysis is done to assess the time-dependent influence of critical parameters in the governing equation for several samples. Finally, thermal conductivity measurements are presented for seven different liquid substances by fitting the thermal model to experimental data across a range of temperatures. Reference correlations are included for comparison. The sample thermal conductivity and ambient temperature of the experimental conditions range from 0.125-16.5$\frac{W}{m\cdot K}$ and 10-400°C, respectively. The total uncertainty, comprised of both the experimental design and fitting process, of all measurements is quantified.

I. INTRODUCTION

In recent years, there has been a marked increase in the quantity and diversity of power generation technologies worldwide. These advanced systems seek to compete in terms of economics, environmental sustainability, and thermal efficiency[1]. Nearly all designs, such as those pertaining to nuclear energy and concentrated solar power (CSP), feature some working fluid to transfer and/or store heat[2,3]. This being the case, it becomes necessary to attain an adept understanding of the thermophysical properties of the fluid in order to develop heat transfer models that govern the system design and performance[4]. Specifically, the Nusselt correlations that describe the convective heat transfer through a liquid, by definition, require an accurate characterization of the thermal conductivity (k) of that material[5,6]. In some Generation IV nuclear reactors and CSP processes, molten salts are used to exchange heat at high temperatures due to their high boiling point and high specific heat[7]. Measuring k of molten salts has shown to be particularly difficult due to their corrosive and electrically conductive nature[8–10].

In the literature, a variety of experimental methods have been presented for measuring k of such liquids. Among these are the variable-gap apparatus, concentric-cylinders, laser flash, transient hot-wire, and parallel-plates[11–15]. The variable-gap apparatus is a steady-state technique that records temperature across a continually changing sample thickness, but it often experiences significant error attributed to heat shunting via paths other than through the liquid[11]. The concentric-cylinders technique assesses the steady-state temperature gradient across a liquid heated by the inner cylinder, and has demonstrated the ability to reduce unwanted convection and thermal radiation via a meticulous crucible design and small gap across the sample[12]. The laser flash technique, which observes the time-dependent diffusion of heat from a pulse-heated disk, through a sample, into a second disk, is intrinsically prone to heat leakage[13]. The transient hot-wire technique heats a sample from an infinite line source and is often favored due to short measurement times and robust thermal models with fully developed error analyses[14]. The parallel-plates technique measures the downward flowing heat flux through a material, but has reported large errors from heat losses in high-temperature liquids[15]. Chliatzou et al.[16] reviews in greater depth the advantages and drawbacks of each of these techniques in terms of measurement accuracy for a variety of high-temperature molten salts, while Magnusson et al. focuses specifically on fluoride salt compounds[7].

In addition to non-conductive heat transfer, electrical conduction from the instrument into the sample can impose measurement errors. Such being the case, some traditional instrumentation techniques for measuring thermophysical properties may be insufficient in their ability to account for both of these sources of error. This work seeks to develop an instrumental method and associated analytical model for measuring the temperature-dependent k of two electrically conductive molten salts. To achieve this, modifications are made to traditional transient hot-wire and concentric-cylinders techniques. Measurements of electrically and non-electrically conductive fluids are also performed to calibrate the usable k range of the technique.

II. METHODS

A. Basis for Measurement Technique

In this study, a novel instrumentation method and thermal analysis model are developed to combine the advantages of

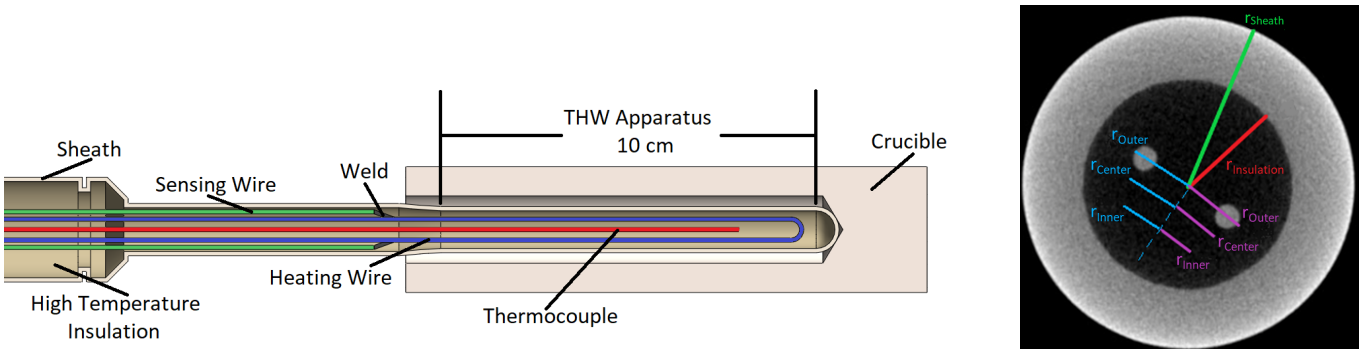

FIG. 1: a) Schematic of the internal components of the needle probe and crucible. Dimensions are not proportionately represented. b) CT scan of a cross-section of the lower end of the needle probe. Dimensions are labeled, where r_{sheath} and $r_{insulation}$ mark the sheath and insulation outer radii, respectively. r_{sheath} is synonymous with r_{probe}, whose measured value is listed in Table I. r_{center}, r_{inner}, and r_{outer} mark the center, inner, and outer radii of the heating wires, respectively

a transient hot-wire (THW) with a concentric-cylinders apparatus. THW is selected for use because it allows for relatively short measurements times and well-established thermal models. The concentric-cylinders method is used as it can minimize undesirable convection and thermal radiation with a small sample volume and careful material finishing. Modifications are made to prevent material corrosion and electrical conduction with the sample.

In the traditional THW technique, a sample is heated from within by inducing a constant heat flux via Joule heating of a thin wire[17]. In the modified technique (MTHW) used here, the apparatus is electrically insulated and sheathed to protect against electrical conduction and corrosion when in contact with the liquid sample. A thermocouple at the centerline of the THW system records the relative temperature rise. This temperature rise is strongly influenced by k of the surrounding medium. If the sample has a low k value, then the temperature near the sensor will increase more rapidly as the fluid is slow to conduct heat away. The opposite effect will occur for samples of high k. THW is beneficial due to the short measurement times associated with thermal transience, which reduces the propensity for natural convection to develop in the liquid sample[14]. However, the additional thermal mass with the MTHW approach results in longer measurement times (tens of seconds, compared to around one second with the THW technique), which is sufficiently long to observe convection.

The concentric-cylinders technique refers to the selected geometry, where the inner and outer cylinders bound the salt sample[18]. Reference data using this steady-state method notes that convection is reduced as the gap between the cylinders decreases[19]. However, if the gap is excessively small, then the technique is prone to become overly sensitive. Furthermore, thermal radiation emissions with the crucible may be reduced by improving the surface finish of the inner wall. This work presents a modification of the concentric cylinder where the inner and outer cylinders are the MTHW apparatus and crucible, respectively, and the transient temperature rise is recorded instead of performing a steady state measurement.

Besides heat transfer considerations, the sensor must limit confounding influences from electrical conduction and material corrosion in the conducting liquids, requiring some adjustments to be made to the traditional THW apparatus. A detailed diagram of this Modified Transient Hot-wire Needle Probe (referred to hereafter as “needle probe”) is seen in Fig. 1a[20–23].

The heating and sensing region of the needle probe (labeled in Fig. 1a as "THW Apparatus") measures 10cm in length and 2.6mm in diameter. It consists of a thermocouple, a heating wire, electrical insulation, and a sheath. The thermocouple is Type K and serves to collect time-domain temperature data at the centerline. The bead of the thermocouple is fixed at both the axial and radial centers of the heating/sensing region (i.e. 5cm from the tip along the centerline). A chromel heating wire loops once through the entire 10cm length of this same region, generating a constant radial heat flux as the leads are supplied with a constant power input. Section II C uses FEM to assess radial to axial heat fluxes. Alumina (Al_2O_3) occupies the majority volume and electrically insulates the thermocouple, heating wire, and sheath from one another to avoid electromagnetic interference (EMI). It also insulates the instrumentation from an electrically conductive sample, such as molten salt. The interior apparatus of the needle probe is protected by a Nickel-200 sheath, which is non-reactive with the otherwise corrosive substances studied in this work[24]. The needle probe was manufactured by Idaho National Laboratory (INL) and has been verified for use up to 400°C, at which point EMI between the thermocouple and heating wire may become more prone to occur[23].

B. Analytical Heat Transfer Model (Multilayered Thermal Quadrupoles in the Time Domain)

Traditional, 1D analytical models for THW instruments evaluate the slope of the linear region of the temperature vs. log(time) profile to extract k of a semi-infinite sample[21]. However, due to the fact that the sample gap is small and the heating is not a line source, a semi-infinite domain may no longer

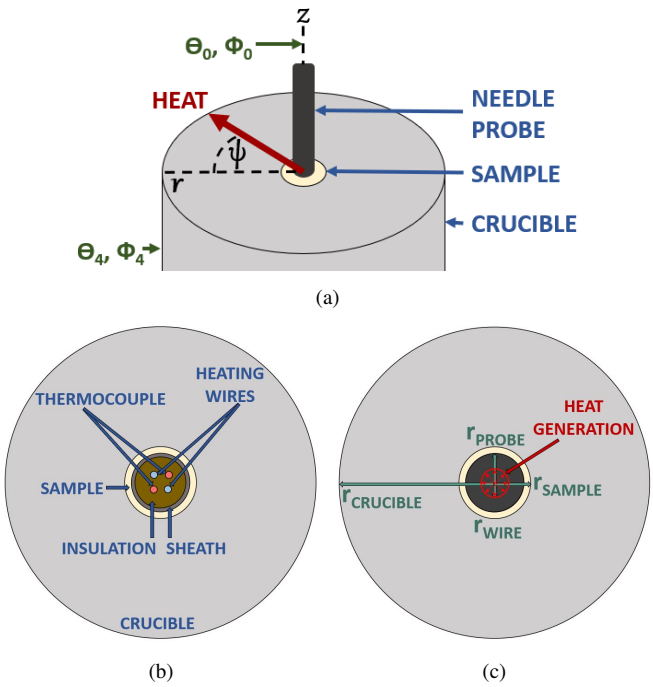

FIG. 2: a) Three-layered geometry of the needle probe, sample, and crucible. Coordinates r, z, and ψ correspond to the radial, axial, and azithumal directions, respectively. 1D (radial) heat conduction is indicated. Definitions of θ_0, ϕ_0, θ_4, and ϕ_4 are presented in the development of Eq. 10. b) Schematic of the true cross-section of the system. c) Representation of the three-layered concentric cylinders used in the analytical model, where the innermost layer is a lumped version of the needle probe properties[29].

be assumed. Therefore, it becomes necessary to develop a new analytical model that can characterize thermal conduction from the needle probe, through the sample, and into the crucible. This model will be fit to the data and used to quantify the thermophysical properties of the sample. In order to simplify the application of the heat diffusion equation and associated boundary conditions to this multilayered geometry (see Figure 2a) and account for the thermal mass of the probe, the method of thermal quadrupoles has been selected to develop the analytical solution along the radial direction[25–28].

In essence, the true needle probe geometry is lumped into one single cylindrical layer (Fig. 2b & 2c). This approach was validated by Hollar et al. and allows heat transfer in the azimuthal (ψ) direction to be neglected in the analytical model[29]. Although heat is asymmetrically generated in the core of the needle probe, the act of lumping the wires, insulation, and sheath assumes that the heat flux has become homogeneous by the time it penetrates outward from the exterior surface of the sheath. The lumped thermal conductivity (k_{probe}) and thermal diffusivity (α_{probe}) are defined in Eq. 1 and Eq. 2, respectively, based on the dimensions and properties of the constituents.

$$k_{Probe} = \frac{ln(\frac{r_{sheath}}{r_{wires}})}{\frac{ln(\frac{r_{insulation}}{r_{wires}})}{k_{insulation}} + \frac{ln(\frac{r_{sheath}}{r_{insulation}})}{k_{sheath}}} \tag{1}$$

$$\alpha_{Probe} = \frac{\mathcal{V}_{sheath}\alpha_{sheath} + \mathcal{V}_{insulation}\alpha_{insulation} + \mathcal{V}_{wires}\alpha_{wires}}{\mathcal{V}_{total}} \tag{2}$$

Eq. 1 was derived using a thermal resistance network, whereas Eq. 2 is the sum of the volumetric weights of each constituent material. The terms r and $\mathcal{V}$ refer to the radius and volume of each material. The thermophysical properties of the constituents were taken from correlations found in the existing literature, while the radii were measured from the computed tomography (CT) scan in Fig. 1b.

Because it is assumed that heat is generated homogeneously at the average outer radius of the wires (Fig. 2c), each of the surrounding layers may be described by the form of the heat diffusion equation shown in Eq. 3.

$$\frac{\delta^2 T}{\delta r^2} + \frac{1}{r}\frac{\delta T}{\delta r} = \frac{1}{\alpha}\frac{\delta T}{\delta t} \tag{3}$$

The thermal quadrupoles technique transforms Eq. 3 from the time domain into the Laplace domain. The new form of the heat diffusion equation is seen in Eq. 4, where θ is the temperature and s is the Laplace parameter.

$$\frac{\delta^2 \theta}{\delta r^2} + \frac{1}{r}\frac{\delta \theta}{\delta r} = \frac{s}{\alpha}\theta \tag{4}$$

Eq. 4 may be rearranged to take the form of a Modified Bessel Equation of order zero. From this, the Laplace temperature may be solved for as seen in Eq. 5, where, I_0 and K_0 are zero-order modified Bessel functions of the first and second kind, respectively. Additionally, $\sigma = \frac{s}{\alpha}$ and c_1 and c_2 are arbitrary constants.

$$\theta = c_1 I_0(\sigma r) + c_2 K_0(\sigma r) \tag{5}$$

The Laplace heat rate (ϕ) is defined by Fourier's Law in Eq. 6, where Γ is a surface area perpendicular to the direction of heat conduction. In this case, because heat conduction is assumed 1D radially, Γ is the axial surface area of a cylindrical layer.

$$\phi = -k\Gamma\frac{d\theta}{dr} \tag{6}$$

The thermal quadrupoles technique adapts Eq. 5 and Eq. 6 to a system of equations bounded by the temperature (θ) and heat rate (ϕ) at the inner and outer surfaces, shown in Eq. 7a. The 2x2 transfer matrix describing the heat conduction through the passive cylindrical layer between these two boundaries contains four "quadrupoles" (A-D), defined in Eq. 7b-7e. A complete derivation of these terms, along with the thermal quadrupoles method in general, is produced by Maillet et al.[25].

$$\begin{bmatrix}\theta_{inner}\\ \phi_{inner}\end{bmatrix} = \begin{bmatrix}A & B\\ C & D\end{bmatrix}\begin{bmatrix}\theta_{outer}\\ \phi_{outer}\end{bmatrix} \tag{7a}$$

$$A = r_o\sqrt{\sigma}(K_1(r_o\sqrt{\sigma})I_0(r_i\sqrt{\sigma}) + K_0(r_i\sqrt{\sigma})I_1(r_o\sqrt{\sigma})) \quad (7b)$$

$$B = \frac{1}{2\pi kL}(K_1(r_o\sqrt{\sigma})I_0(r_i\sqrt{\sigma}) + K_0(r_i\sqrt{\sigma})I_1(r_o\sqrt{\sigma})) \quad (7c)$$

$$C = 2\pi kLr_ir_o\sigma(I_1(r_o\sqrt{\sigma})K_1(r_i\sqrt{\sigma}) - I_1(r_i\sqrt{\sigma})K_1(r_o\sqrt{\sigma})) \quad (7d)$$

$$D = r_i\sqrt{\sigma}(I_0(r_o\sqrt{\sigma})K_1(r_i\sqrt{\sigma}) + I_1(r_i\sqrt{\sigma})K_0(r_o\sqrt{\sigma})) \quad (7e)$$

The terms r_i, r_o, and L refer to the inner radius, outer radius, and length of each passive cylindrical layer. All other terms have been defined previously. In addition to the quadrupoles matrix describing heat transfer through a single annular layer, the conduction at the interface of two layers (e.g. needle probe-sample and sample-crucible) must also be characterized. This is done using a transfer matrix representing thermal contact resistance (R_c), shown in Eq. 8, and derived by Maillet et al.[25].

$$\begin{bmatrix}\theta_{Layer1}\\ \phi_{Layer1}\end{bmatrix} = \begin{bmatrix}1 & R_c\\ 0 & 1\end{bmatrix}\begin{bmatrix}\theta_{Layer2}\\ \phi_{Layer2}\end{bmatrix} \quad (8)$$

Similarly, the external free convection between the crucible surface and the ambient air may be accounted for, as shown below.

$$\begin{bmatrix}\theta_{Layer1}\\ \phi_{Layer1}\end{bmatrix} = \begin{bmatrix}1 & 0\\ h\Gamma_{crucible} & 1\end{bmatrix}\begin{bmatrix}\theta_{Layer2}\\ \phi_{Layer2}\end{bmatrix} \quad (9)$$

The complete governing equation for the analytical model may now be written (Eq. 10), which describes the 1D, transient conductive heat transfer from the centerline of the needle probe to the external air. Subscripts 0, 1, 2, 3, and 4 denote the centerline, lumped needle probe, liquid sample, crucible, and external air at an infinite distance, respectively.

$$\begin{bmatrix}\theta_0\\ \phi_0\end{bmatrix} = \begin{bmatrix}A_1 & B_1\\ C_1 & D_1\end{bmatrix}\begin{bmatrix}1 & R_{c1-2}\\ 0 & 1\end{bmatrix}\begin{bmatrix}A_2 & B_2\\ C_2 & D_2\end{bmatrix}\begin{bmatrix}1 & R_{c2-3}\\ 0 & 1\end{bmatrix}\begin{bmatrix}A_3 & B_3\\ C_3 & D_3\end{bmatrix}\begin{bmatrix}1 & 0\\ h\Gamma_{crucible} & 1\end{bmatrix}\begin{bmatrix}\theta_4\\ \phi_4\end{bmatrix} \quad (10)$$

The bounding temperatures and heat rates are related by the thermophysical properties and geometry of each successive annulus. The centerline heat rate (ϕ_0) is the *Power* applied to the heating wire. The external temperature (θ_4) is implicitly solved for in the process of evaluating the system of two equations to isolate a single solution for the centerline temperature (θ_0). θ_0 is not absolute and instead demonstrates a relative rise above the initial temperature of the system at thermal equilibrium. The external heat rate (ϕ_4) is taken to be 0 by convention of the thermal quadrupoles technique. Due to the complexity of this system of equations, a numerical Laplace inversion is used to solve the centerline temperature (T_0) against the logarithm of time. This solution generates the curve that will be fit to the experimental data.

TABLE I: Parameters used in both the finite-element and analytical models. The sample and crucible are water and SS316, respectively, at 20°C. The source of the listed quantity is provided in brackets. Calipers were used to measure r_{sample}, $r_{crucible}$, L. *Power* was measured with a multimeter.

Parameter	Value
r_{probe}	1.3 mm [Fig. 1b]
k_{probe}	47 W/(m·K) [Eq. 1]
α_{probe}	15 mm^2/s [Eq. 2]
R_{c1-2}	10^{-8} K·m^2/W [17]
r_{sample}	1.98 mm
k_{sample}	0.6 W/(m·K) [31]
α_{sample}	0.15 mm^2/s [31]
$r_{crucible}$	12.7 mm
$k_{crucible}$	15.3 W/(m·K) [COMSOL]
$\alpha_{crucible}$	3.82 mm^2/s [COMSOL]
h	10 W/(m^2·K) [19]
L	100 mm
Power	0.95 W

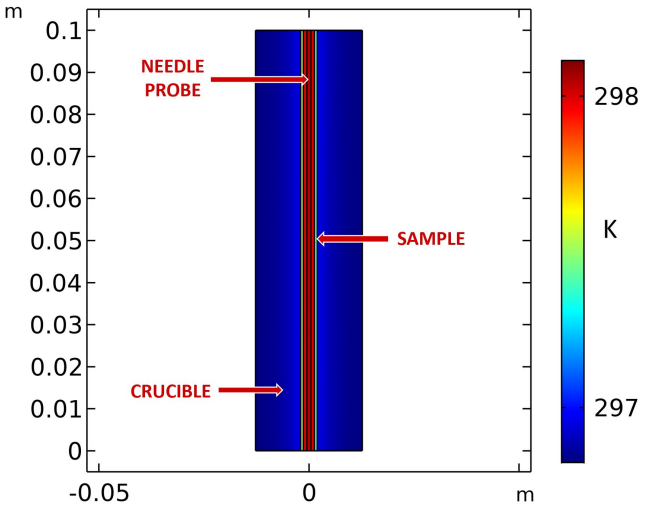

FIG. 3: 2D slice of an axisymmetric 3D finite-element model of the needle probe in 293 K water, surrounded by a steel crucible. The color gradient represents temperature (Kelvin). This simulation was performed in COMSOL Multiphysics.

C. Validation of the Thermal Quadrupoles Solution Using a Finite-Element Model

A three-dimensional (3D) axisymmetric finite-element model was made using COMSOL Multiphysics to evaluate agreement with the thermal quadrupoles solution. The thermophysical properties were obtained either from reference sources in the literature or COMSOL itself, as noted in Table I. The dimensions of the needle probe were determined from the CT scan in Fig. 1b. For the finite-element model, a 3D axisymmetric domain was constructed (see Fig. 3), with a centerline heating element, lumped needle probe, water sample, and Stainless Steel 316 crucible. A vertical wall convective heat flux was applied to the outer boundary of the crucible, with insulation on the top and bottom of the system. Laminar

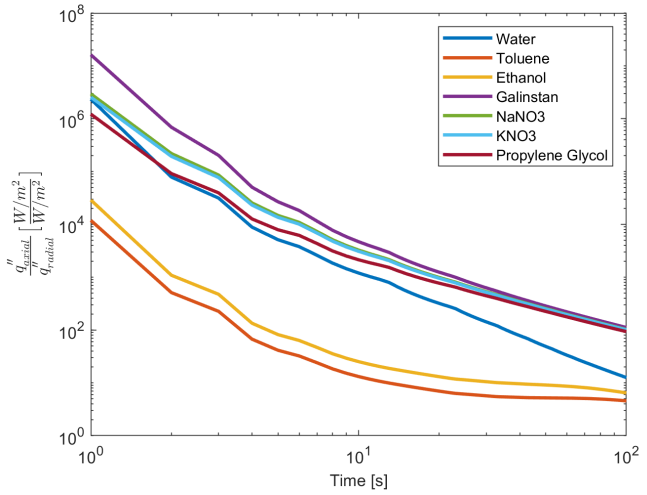

FIG. 4: Finite-element simulation showing the ratio of radial to axial heat fluxes ($\frac{q''_{radial}}{q''_{axial}}$) over 100 seconds. The 3D COMSOL model was constructed as in Fig. 3 using seven sample materials.

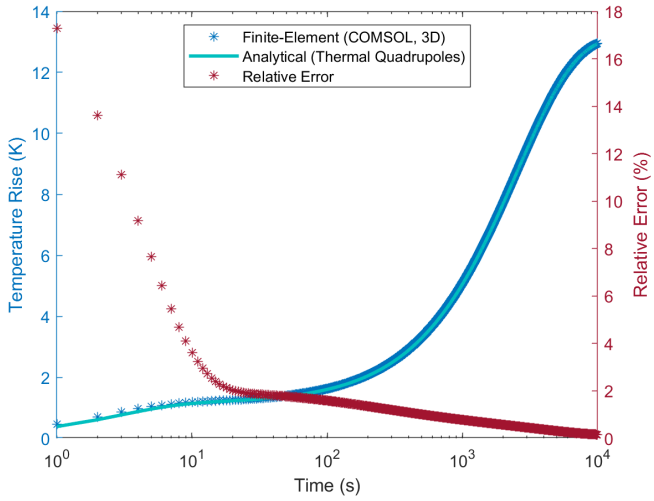

FIG. 5: Time-domain temperature profile at the centerline of the needle probe. Comparison of the finite-element and analytical (thermal quadrupoles) models. Relative error between the two is also shown.

flow was applied to the thin water layer with an atmospheric pressure point constraint applied at the top. The ratio of radial heat flux to axial heat flux ($\frac{q''_{radial}}{q''_{axial}}$) was assessed against time in Fig. 4 for water, sodium nitrate, potassium nitrate, toluene, ethanol, propylene glycol, and galinstan samples. It is seen that as time increases, the amount of heat conducting axially increases relative to that conducting radially. It is noted that the quicker decrease of the ratio in less conductive fluids (e.g. toluene, ethanol, and propylene glycol) may introduce experimental error as the analytical model assumption of 1D radial heat transfer could be comprised.

The analytical quadrupole solution was assessed against the finite-element model, both using the parameter values in Table I. The analytical model was evaluated using a custom MATLAB program. The results are shown in Fig. 5. The time-domain temperature profiles produced by each model demonstrate a very strong agreement. The agreement is quantified by the relative error curve.

In early time regimes, the relative error may be significant, though it decreases substantially as time increases. This means that the fitting of the analytical model to the experimental data will be more prone to error in early time regimes where the analytical model deviates from the finite-element profile. This is likely due to the assumption of a lumped mass for the needle probe.

D. Parameter Sensitivity Analysis

A parameter sensitivity analysis was performed to evaluate the time regimes in which each material property and geometric feature have the greatest influence on the centerline temperature profile. Each selected parameter from Eq. 10 was individually reduced by 5%. The percent change in slope ($\frac{dT}{dt}$) between the nominal and varied solutions is shown in Fig. 6a.

The sample used in Fig. 6a is water, whose k value at the given temperature is 0.594 $\frac{W}{m \cdot K}$. The results indicate that the strength of influence of each parameter rises and falls sequentially with the conducting flow of heat. In other words, at early time intervals (<10^1 seconds), when the heat has not yet penetrated outward from the needle probe, the thermophysical properties of the needle probe (k_{probe} and α_{probe}) dominate. At intermediate time intervals (10^1-10^2 seconds), the sample properties (k_{sample} and α_{sample}) reach their peak influence. At longer times (>10^2 seconds), $k_{crucible}$ and $\alpha_{crucible}$ bear greater influence, and finally give way to the convective heat transfer coefficient (h) as time moves towards infinity. For the first $\sim 10^3$ seconds, the heating power is the most sensitive parameter.

To understand the parametric sensitivity of other samples, whose k is significantly lower or higher than that of water, two additional analyses were performed. The results for liquid toluene (k=0.133 $\frac{W}{m \cdot K}$) and galinstan (k=16.5 $\frac{W}{m \cdot K}$) are presented in Fig. 6b & 6c, respectively.

Similar to the results in Fig. 6a, the sensitivity of each parameter rises and falls as the heat propagates through that layer of the system. When using toluene, it is seen that k_{probe}, α_{probe}, k_{sample} and α_{sample} all exhibit increased sensitivity relative to the water simulation in the time span of 10^1-10^2 seconds.

The results of the galinstan test differ more significantly from those of water and toluene. After just $\sim$ 0.2 seconds, $k_{crucible}$ and $\alpha_{crucible}$ quickly rise to be the most sensitive parameters (along with Power). After 10^3 seconds, external convection also rises to strong influence.

The sensitivity analysis of $NaNO_3$ is very similar to that of water in terms of when k_{sample} achieves peak sensitivity (10^1 seconds). k_{probe} and α_{probe} also reach their climaxes at this time, though to a lesser degree.

It may now be seen that thermophysically different samples

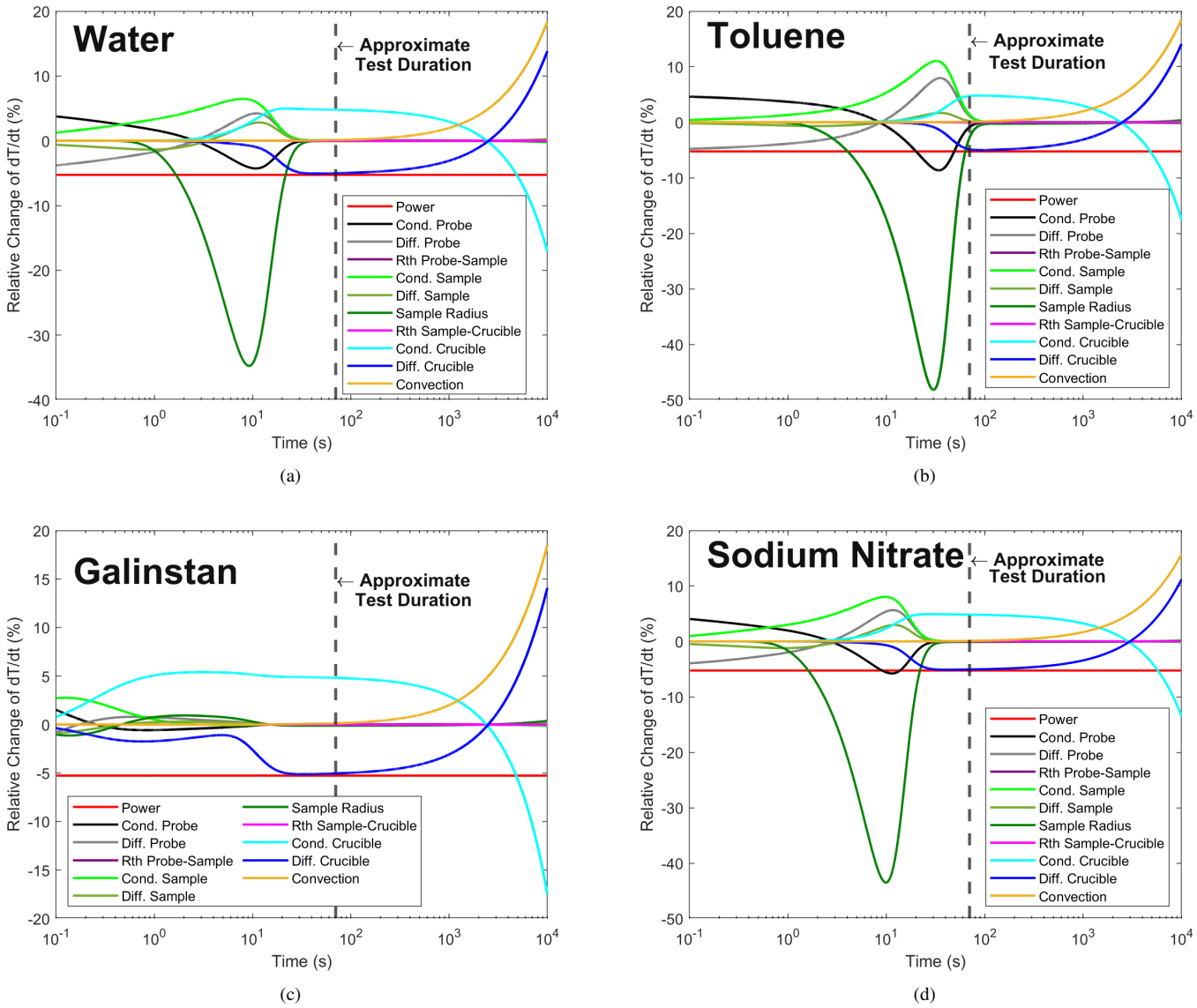

FIG. 6: Sensitivity analyses for a three-layered thermal quadrupoles analytical model. The three layers are the needle probe, sample, and crucible. The crucible material is Stainless Steel 316 containing a) water (moderate k, low $T_{initial}$), b) toluene (low k, low $T_{initial}$), and c) galinstan (high k, low $T_{initial}$), and d) $NaNO_3$ (moderate k, high $T_{initial}$)

may yield drastic effects on the sensitivity of each parameter in the governing equation. These trends may provide insight on the experimental results (Section IV) in terms of goodness of fit, sources of error, and limitations of the needle probe.

III. EXPERIMENTAL DESIGN

The needle probe, test sample, and crucible were brought to the initial test temperature in a Sentry Xpress 5.0 furnace, as depicted in Fig. 7a. For materials with a low flash point (e.g. toluene and ethanol), a Cole-Parmer Polystat Heated Circulating Bath was substituted for the furnace (Fig. 7b). Heated water was circulated through copper tubing tightly coiled around the crucible throughout the duration of the experiment. The initial temperatures were randomly ordered from one test to the next. A stand supported the needle probe positioned within the crucible. To simplify the presentation of the experimental process, it has been consolidated into a block diagram in Fig. 7c.

Heating power for the needle probe was supplied by an Accel Instruments TS200 Power Supply. For each test, a constant voltage between 1V to 5V was applied, resulting in 0.24-5.95 W based on a heating wire resistance measured to be 4.2 Ω. Several tests were performed at each initial temperature using multiple voltages. The thermal flux from the heating wires conducts radially outwards, increasing the temperature of the needle probe, sample, and crucible. A National Instruments

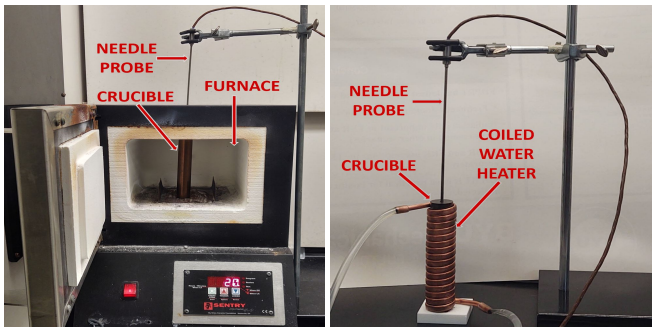

(a) (b)

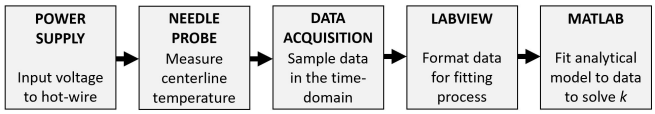

(c)

FIG. 7: a) A furnace controls the initial and ambient temperature during testing, with the needle probe inserted through an orifice in the top to be immersed in the sample. b) A copper-coiled loop of heated water controls the system temperature for samples with a low flash point. c) Block diagram of experimental procedure for time-domain measurements. The arrows represent the end-to-end process from heat generation to k measurement.

9213 Temperature Input Module sampled the temperature data from the thermocouple at 50 Hz, and was recorded using LabVIEW. To maintain the integrity of the 1D radial heat transfer assumption in the analytical model (Sections II B & II C), data collection did not exceed a duration of approximately 70 seconds.

IV. MEASUREMENT RESULTS

This work seeks to evaluate the ability of the needle probe to measure k of several reference liquids. First, a brief discussion will be on the fitting process and uncertainty analysis in Sections IV A & IV B, respectively. Then, the results of the temperature-dependent k measurements for each of the seven liquid samples tested in this study will be presented in Section IV C. The subsection for each sample contains a plot showing the experimentally measured k values across several temperatures. A first-order line of best fit is included to indicate the temperature-dependent trend of the data. Below each plot is a table, listing the measured value (k_{Meas}) and reference value (k_{Ref}) at each temperature alongside the error bar size determined from the uncertainty analysis (μ_{total}).

A. Fitting

The analytical model was fit to the temperature rise data using a custom MATLAB code that operates using the Levenberg-Marquardt algorithm[30,31]. The parameters k_{sample} and α_{sample} were varied with each iteration until reaching a best fit based on the minimum achievable χ^2 error. The best fit k_{sample} was taken to be the experimentally measured value. A representation of this fitting process is shown in Fig. 8 using a water sample. The trends seen are consistent across all samples. Additional plots may be found in Appendix A.

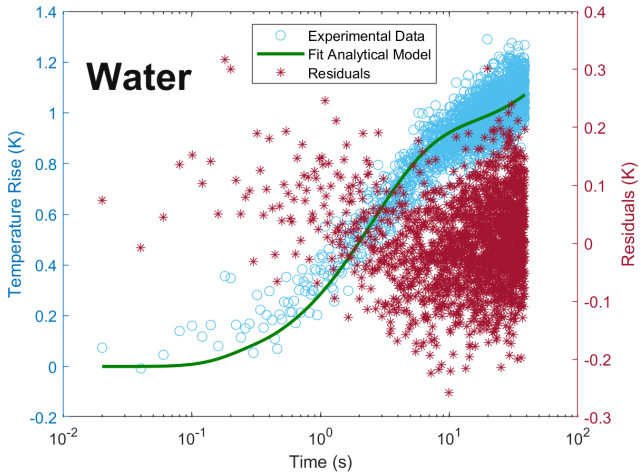

FIG. 8: Representative best fit plot using a water sample with $T_{initial}$=40°C and $Power$=0.95W.

The representative plot demonstrates that the analytical model is able to fit the data reasonably well. However, it is observed that in early time regimes (<10^0s), the model deviates slightly from the data. Based on the parameter sensitivity analysis (Fig. 6a), the dominant parameters in such early time frames are P, k_{probe}, and α_{probe}. To investigate possible error in P (power), testing was done to verify the accuracy of the voltage input from the Accel Instruments TS200 Power Supply. No significant uncertainty was measured, so the fit deviation is thus attributed to uncertainty in the thermophysical properties of the needle probe constituents (e.g. k_{probe} and α_{probe}). It is noted that this uncertainty does not imply significant uncertainty in measurements of k_{sample}. This reasoning is also derived from the findings presented in Section II D. In regions where $10^0 s < time < 10^2 s$, k_{sample} reaches its peak sensitivity, whose value is greater than that of k_{probe} and α_{probe}. The stronger fit of the model to the data in this time region suggests greater confidence in the measurements of k_{sample}.

B. Uncertainty Analysis

In order to quantify the uncertainty (μ) associated with each data point, a Monte Carlo (MC) analysis was performed. Each parameter in the analytical model was assigned to a Gaussian distribution, whose mean is the nominal value, and whose standard deviation is the root-sum-of-squares of random uncertainty in the data and systematic uncertainty in the parameter due to the instrumentation. An assumed uncertainty of 5% of the nominal value was made if the systematic bias was not published in the literature for any hardware and/or software components. The MC analysis was iterated until the de-

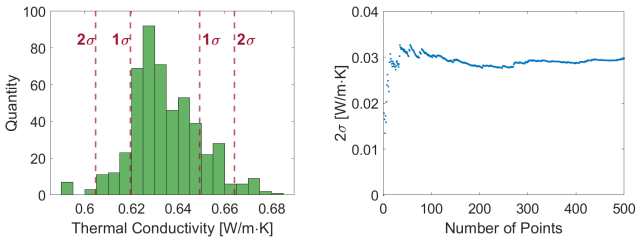

FIG. 9: Left: Histogram of measured k values for the H_2O test seen in Fig. 8. 1σ and 2σ mark the first and second standard deviations, respectively. Right: Convergence of 2σ after 500 iterations.

viation between iterations converged. The total experimental uncertainty (μ_{total}) is taken as $\mu_{total} = \sqrt{\mu_{MC}^2 + \mu_{\chi^2}^2}$, where μ_{MC} is the instrumental uncertainty and μ_{χ^2} is the χ^2 fitting error. This is the size of the error bar above and below the nominal value of the given data point with a 95% confidence interval. An exemplar MC analysis is given in Fig. 9 to represent a distribution of k_{sample} values and verify convergence. The temperature rise data used is the same as that presented in Fig. 8. Additional MC analyses for each sample may be found in Appendix A.

The histogram of measured k values from the MC uncertainty analysis demonstrates an apparently Gaussian distribution with a slight skew. This is consistent across every sample and temperature.

C. Results by Sample

1. Water (H_2O)

The first-order trend line based on the data taken in the furnace (Fig.7a) aligns approximately tangentially with the reference correlation. Ramires et al. develops the quadratic reference correlation based on unsmoothed absolute measurements gathered using primary experimental apparatus with complete working equations[32]. Relative to the reference correlation, the average root-mean-square error (RMSE) of the experiments with the needle probe is $0.026\frac{W}{m\cdot K}$ (4.01%)

TABLE II: Experimental results for measuring H_2O in the temperature range of 25-70°C.

$T_{Initial}[°C]$	$k_{Meas}[\frac{W}{m\cdot K}]$	$k_{Ref}[\frac{W}{m\cdot K}]$	$\mu_{total}[\frac{W}{m\cdot K}]$
25	0.65	0.60	0.038 (5.8%)
30	0.62	0.61	0.026 (4.2%)
40	0.60	0.63	0.030 (4.9%)
50	0.66	0.64	0.039 (5.9%)
60	0.67	0.65	0.028 (4.2%)
70	0.66	0.66	0.041 (6.2%)

As discussed in Section III, two approaches are used in this work for heating the samples. Water was tested using both to establish any potential bias they may be introduced by the alternative copper-coiled water heater. The results indicate that

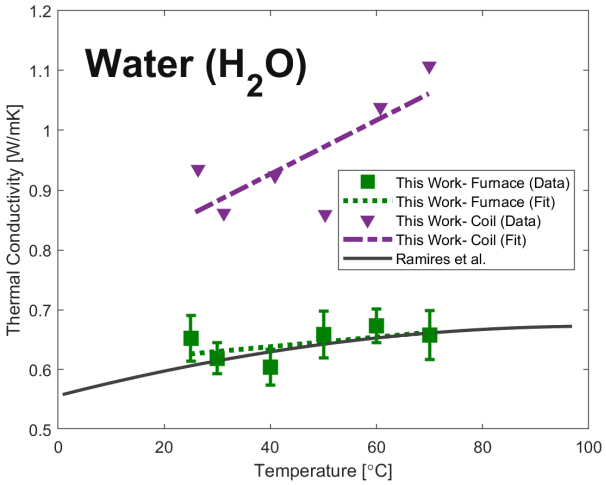

FIG. 10: Comparison of the measured k of H_2O against a reference correlation[32]. Data was collected using both temperature control techniques presented in Section III.

k_{water} is most accurately measured using the furnace, while the coiled heater overestimates the measurement. See Sections IV C 4 and IV C 5 for further discussion on this topic.

2. Sodium Nitrate ($NaNO_3$)

The measurements of k_{NaNO_3} are presented in Fig. 11, with the melting and decomposition temperatures labeled at 310°C and 396°C, respectively. The solid black line, developed by Chliatzou et al., is the primary reference[16]. Their data represents an amalgamation of measurements using THW, pulse-heated flat plate, concentric-cylinders, and wave-front interferometer techniques. The overall uncertainty declared at the 95% confidence level is 7% for the reference correlation. The correlation from Zhao et al. (dashed blue line) was recently produced using a 3ω hot-wire technique and is included as a secondary reference[33].

All measured values of k_{NaNO_3} from this work (shown in green) fall between the two reference correlations. The first-order trend line demonstrates a negative temperature dependence, whose slope approximately agrees with those of Chliatzou et al. and Zhao et al. It is acknowledged that some past correlations for $NaNO_3$ found in the literature and reviewed by Chliatzou et al. have demonstrated an erroneous positive temperature-dependence. The downward trend of the needle probe measurements thus increases confidence in its ability to accurately measure electrically conductive liquid salts at elevated temperatures. The average RMSE relative to Chliatzou et al. is $0.046\frac{W}{m\cdot K}$ (8.89%).

3. Potassium Nitrate (KNO_3)

The KNO_3 data are plotted in Fig. 12, with melting and decomposition temperatures labeled at 334°C and 550°C, re-

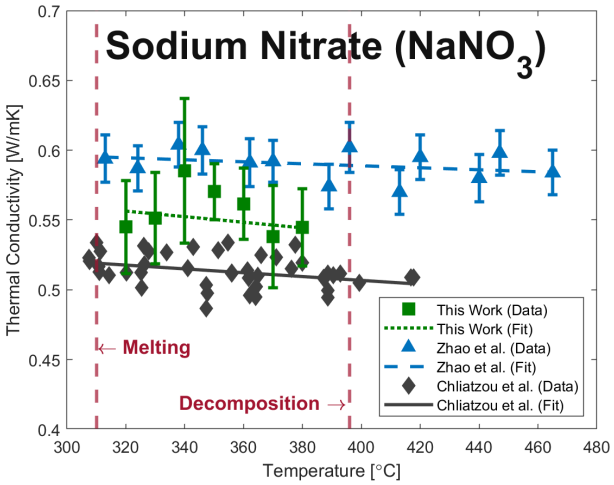

FIG. 11: Comparison of the measured k of molten $NaNO_3$ against two reference correlations[16,33]. Temperatures were controlled using a furnace.

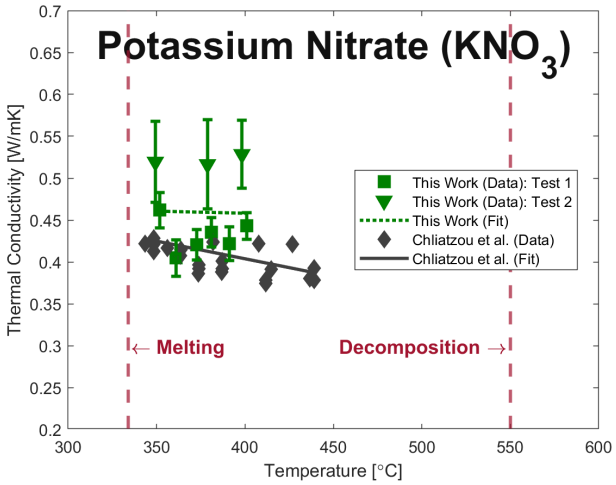

FIG. 12: Comparison of the measured k of KNO_3 against a reference correlation[16]. Temperatures were controlled using a furnace.

TABLE III: Experimental results for measuring $NaNO_3$ in the temperature range of 320-380°C.

$T_{Initial}[°C]$	$k_{Meas}[\frac{W}{m\cdot K}]$	$k_{Ref}[\frac{W}{m\cdot K}]$	$\mu_{total}[\frac{W}{m\cdot K}]$
320	0.55	0.52	0.033 (6.1%)
330	0.55	0.52	0.033 (5.9%)
340	0.59	0.52	0.052 (8.8%)
350	0.57	0.51	0.020 (3.5%)
360	0.56	0.51	0.025 (4.5%)
370	0.54	0.51	0.037 (6.8%)
380	0.54	0.51	0.028 (5.1%)

TABLE IV: Experimental results for measuring KNO_3 in the temperature range of 350-400°C.

$T_{Initial}[°C]$	$k_{Meas}[\frac{W}{m\cdot K}]$	$k_{Ref}[\frac{W}{m\cdot K}]$	$\mu_{total}[\frac{W}{m\cdot K}]$
349	0.52	0.43	0.048 (9.3%)
352	0.46	0.42	0.021 (5.2%)
361	0.40	0.42	0.022 (5.4%)
373	0.42	0.42	0.018 (4.3%)
379	0.52	0.41	0.053 (10%)
381	0.44	0.41	0.017 (4.0%)
391	0.42	0.41	0.020 (4.7%)
398	0.53	0.40	0.041 (7.7%)
401	0.44	0.40	0.016 (3.6%)

spectively. Chliatzou et al. developed the correlation in a similar manner as that used for $NaNO_3$[16]. The data was gathered using the THW, pulse-heated flat plate, laser flash, and concentric-cylinders methods with a reported uncertainty of 15% for the reference correlation. The RMSE is calculated to be $0.068\frac{W}{m\cdot K}$ (16.5%).

The measured k_{KNO_3} fit demonstrates a negative temperature dependence, though the slope is more positive than that defined by Chliatzou et al. Data was collected in two testing sessions. Test 1 was done prior to testing most of the other six samples, while Test 2 was after. The higher error in Test 2 is attributed to surface aberrations in the crucible due to oxidation and residual particulates from prior experiments that could not be resolved.

4. *Toluene (C_7H_8)*

The resultant data for toluene over seven temperatures is plotted in Fig. 13. The reference correlation was developed by Ramires et al. from measurements that used both bare platinum and tantalum-coated THW[34]. The polynomial correlation was derived using a least-squares analysis with weighted uncertainties. The overall reported uncertainty of this correlation for the temperature range of interest in this work is 1%. The average RMSE among all seven points measured by this study compared to Ramires is $0.034\frac{W}{m\cdot K}$ (26.00%).

The first-order fit to the measurements from this work trends upwards with temperature, contrary to that suggested by Ramires et al. This may be explained by referring to Fig. 4, which reveals that the relatively low $k_{C_7H_8}$ causes a greater portion of heat to propagate in the axial direction. Consequently, the assumption of 1D radial thermal conduction in the governing equation may be compromised at earlier times than more conductive samples (e.g. H_2O, $NaNO_3$, and KNO_3). As such, greater error is prone to be introduced in measurements.

Additionally, the heating mechanism may introduce unwanted error. As described in Section III, C_7H_8 was heated using a coiled water flow external to the crucible. This modified apparatus could not be accounted for in the analytical model due to complications involving internal flow convection within the coil and R_c between the crucible and coils. Fitting Eq. 10 to this altered system contributes to the overall error, as can be seen in the tests done with water in Section IV C 1. Further development of the quadrupole model would be necessary if this heating setup is used.

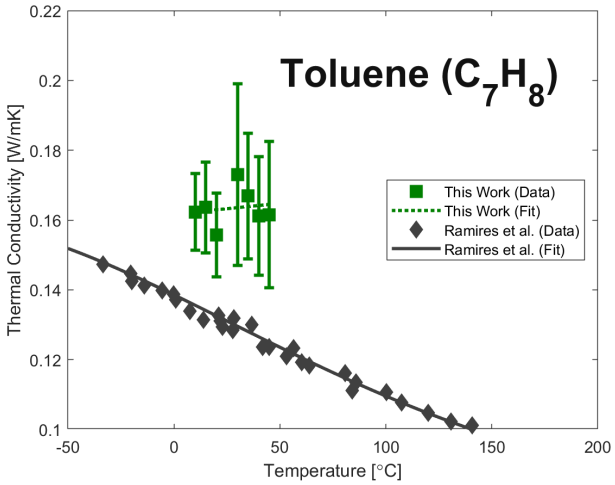

FIG. 13: Comparison of the measured k of C_7H_8 against a reference correlation[34]. Temperatures were controlled using a copper-coiled water heater.

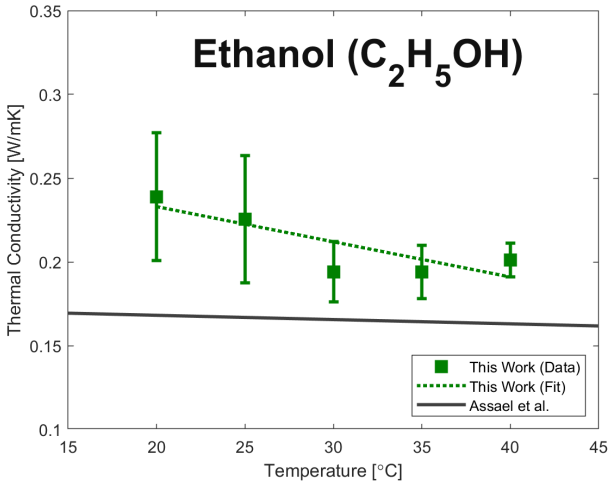

FIG. 14: Comparison of the measured k of C_2H_5OH against a reference correlation[35]. Temperatures were controlled using a copper-coiled water heater.

TABLE V: Experimental results for measuring C_7H_8 in the temperature range of 10-45°C.

$T_{Initial}[°C]$	$k_{Meas}[\frac{W}{m\cdot K}]$	$k_{Ref}[\frac{W}{m\cdot K}]$	$\mu_{total}[\frac{W}{m\cdot K}]$
10	0.16	0.14	0.011 (6.8%)
15	0.16	0.13	0.013 (7.9%)
20	0.16	0.13	0.012 (7.6%)
30	0.17	0.13	0.026 (15%)
35	0.17	0.13	0.018 (11%)
40	0.16	0.13	0.017 (11%)
45	0.16	0.13	0.021 (13%)

TABLE VI: Experimental results for measuring C_2H_5OH in the temperature range of 20-45°C.

$T_{Initial}[°C]$	$k_{Meas}[\frac{W}{m\cdot K}]$	$k_{Ref}[\frac{W}{m\cdot K}]$	$\mu_{total}[\frac{W}{m\cdot K}]$
20	0.24	0.17	0.038 (16%)
25	0.23	0.17	0.038 (17%)
30	0.19	0.17	0.018 (9.3%)
35	0.19	0.16	0.016 (8.3%)
40	0.20	0.16	0.010 (5.0%)

5. Ethanol (C_2H_5OH)

The reference correlation for $k_{C_2H_5OH}$ shown in Fig. 14 was taken from Assael et al.[35]. It is the summation of three distinct contributors, namely the dilute-gas limit (two-body interactions), critical enhancement (long-range density variance near the critical point), and the residual property (many-body collisions and molecular-velocity correlations). The total uncertainty for the primary data is 4.6%.

The trendline fitting the results of this work decreases with increasing temperature. While this is in agreement with Assael et al., the slope is significantly more negative. The RMSE is $0.048\frac{W}{m\cdot K}$ (29.10%). The relatively high error is likely caused by reasons similar to those for toluene discussed in Section IV C 4. These include increased axial heat transfer due to a low $k_{C_2H_5OH}$ and the analytical model complications arising from the alternative heating apparatus (Fig. 7b).

6. Propylene Glycol ($C_3H_8O_2$)

In the literature, studies of $k_{C_3H_8O_2}$ often focus on the inclusion of suspended nanoparticles for improving heat transfer performance of the compound working fluid. To assess the thermal characteristics of pure $C_3H_8O_2$, the reference correlation was taken from the Design Institute for Physical Properties (DIPPR)[36]. DIPPR reports the amalgamation of all primary data with an uncertainty of < 3%. The data from this work estimate $k_{C_3H_8O_2}$ with an RMSE average of $0.039\frac{W}{m\cdot K}$ (19.59%) relative to DIPPR. As the sample has a lower thermal conductivity like C_7H_8 and C_2H_5OH (Sections IV C 4-IV C 5), axial heat transfer contributes some to error (see Figure 4). From the data taken using the coiled heater, a positive temperature dependence is observed, which is likely due to convection in the water loop that is not accounted for in the analytical model. The furnace data more accurately demonstrates a best fit trend is negative, whose slope strongly agrees with that of the reference.

TABLE VII: Experimental results for measuring $C_3H_8O_2$ in the temperature range of 25-52°C.

$T_{Initial}[°C]$	$k_{Meas}[\frac{W}{m\cdot K}]$	$k_{Ref}[\frac{W}{m\cdot K}]$	$\mu_{total}[\frac{W}{m\cdot K}]$
26	0.24	0.20	0.025 (10%)
42	0.23	0.20	0.032 (14%)
52	0.24	0.20	0.044 (18%)

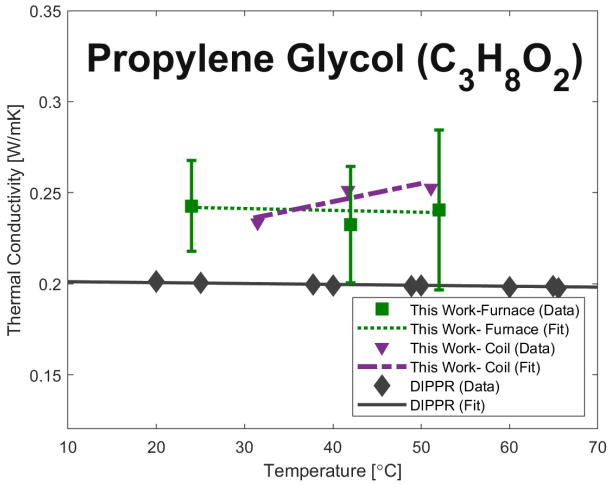

FIG. 15: Comparison of the measured k of $C_3H_8O_2$ against a reference correlation[36]. Data was collected using both temperature control techniques presented in Section III.

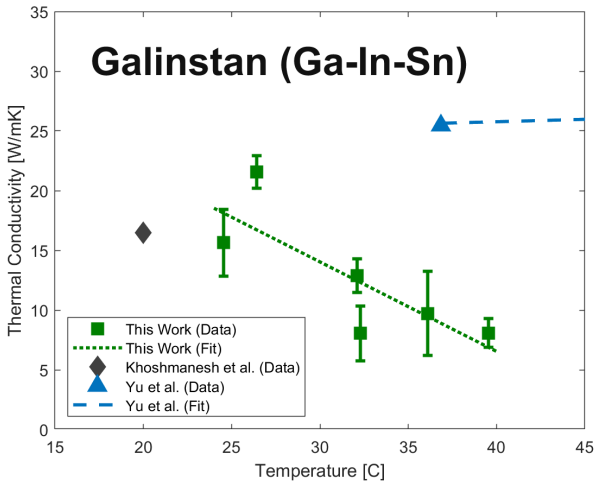

FIG. 16: Comparison of the measured k of GaInSn against a reference correlation[37]. Temperatures were controlled using a furnace.

7. *Galinstan (68.5% Ga, 21.5% In, 10% Sn)*

While many thermophysical property studies have been conducted on galinstan samples, a literature review revealed a dearth of data for the specific composition used in this work (68.5% Ga, 21.5% In, 10% Sn). Khoshmanesh et al., the primary reference, declares a singular value of k_{GaInSn}=16.5$\frac{W}{m\cdot K}$ at room temperature for this composition[37]. This being the case, all measurements in this work were performed at or near room temperature under the assumption that k_{GaInSn} only nominally varies across a limited temperature range. Such is demonstrated by Yu et al., a secondary reference, who developed a correlation for a galinstan composition of (77.2% Ga, 14.4% In, 8.4% Sn)[38]. The RMSE calculated for galinstan (68.5% Ga, 21.5% In, 10% Sn) is 6.17$\frac{W}{m\cdot K}$ (37.37%). The measured $k_{Galinstan}$ underpredicts the reference and trends downward with temperature. Also, it yielded the highest RMSE among all seven samples. This may be explained by the results of the sensitivity analysis in Fig. 6c. The region of peak sensitivity for k is <1 second. The analytical model cannot accurately measure k in such small time frames, and therefore it is not recommended that such highly conductive samples be used with the needle probe.

TABLE VIII: Experimental results for measuring 68.5Ga-21.5In-10Sn in the temperature range of 25-40°C.

$T_{Initial}[°C]$	$k_{Meas}[\frac{W}{m\cdot K}]$	$k_{Ref}[\frac{W}{m\cdot K}]$	$\mu_{total}[\frac{W}{m\cdot K}]$
25	15.7	16.5	2.80 (17.9%)
26	21.6	16.5	1.37 (6.33%)
32	12.9	16.5	1.41 (11.0%)
32	8.05	16.5	2.28 (28.4%)
36	9.71	16.5	3.52 (36.2%)
40	8.08	16.5	1.21 (15.0%)

D. Comments on Thermal Radiation

Because the needle probe operates during time regimes of thermal transience, a temperature disparity will inevitably occur between the bounds of the sample. The surface of the needle probe will be hotter than the interior wall of the crucible, which will drive thermal radiation through the semi-transparent medium in addition to conduction. The Stefan-Boltzmann law defines this net radiative heat flux as $q"_R = \varepsilon\sigma(T^4_{sheath} - T^4_{crucible})$. While radiative effects may be somewhat dampened at low temperatures, even a relatively small temperature difference between the two surfaces at high temperatures may induce significant thermal radiation. This is of particular concern for $NaNO_3$ and KNO_3, which were tested over 300°C (573K). For both salts, there were several instances in which $k_{Meas} > k_{Ref}$. This may be explained by the fact that the governing equation (Eq. 10) assumes that for a given temperature gradient across the sample ($\frac{dT}{dr}$), all heat is transferred through 1D radial conduction ($q"_{C,gov}$). In reality, the heat is transferred via parallel conduction ($q"_{C,par}$) and radiation ($q"_{R,par}$). It can now be stated that for a given heat flux emanating from the needle probe ($q"_{Total}$):

$$q"_{C,gov} > q"_{Total} = q"_{C,par} + q"_{R,par} \tag{11}$$

By Eq. 11, it is easily understood that the analytical model overestimates the amount of heat conducting through the sample for a given $\frac{dT}{dr}$. By Fourier's Law, $q"_C = -k\frac{dT}{dr}$, k_{sample} is overestimated as well. It is largely for this reason that $k_{Meas} > k_{Ref}$ for several high-temperature $NaNO_3$ and KNO_3 measurements. Future quadrupole models for even higher temperature fluids will need to account for radiative heat losses.

V. CONCLUSION

This work innovates existing THW techniques by merging a MTHW needle probe instrument with the concentric-cylinders method for time-domain measurements. Experimental data demonstrates that the needle probe produces measurements with greatest accuracy for liquid samples whose k values range from 0.40 to at least $0.66\frac{W}{m\cdot K}$. Measurements of high-temperature, electrically conductive molten salts in this range are accurately measured with slight overestimations due to thermal radiation. The k of lowly conductive materials is overestimated due to increased axial heat transfer. Volatile liquids that were heated using the alternative coiled water loop demonstrated increased error as this temperature control method is not valid given the model constraints. The k of one highly conductive sample was underestimated due to the limited time of sensitivity in the model. The MTHW needle probe design has performed well in corrosive and electrically conductive molten salts, namely $NaNO_3$ and KNO_3.

Preparations are currently being made to apply this needle probe technique to high-temperature molten fluoride salts. Of particular interest are LiF-NaF-KF and LiF-BeF_2, both of which are corrosive and electrically conductive, with melting points above 450°C (723K). As noted in Section IV D, thermal radiation should be accounted for at such elevated temperatures to improve the accuracy of k measurements. A modified analytical model which can produce a governing equation that accounts for parallel conduction and radiation is being sought.

ACKNOWLEDGMENTS

Funding for this research has come from the Department of Energy, Nuclear Energy University Program (NEUP): Award #19-17413, the Nuclear Regulatory Commission: Award #31310019M0006, and the NEUP Graduate Fellowship.

DATA AVAILABILITY STATEMENT

Data is available upon request by emailing troy.munro@byu.edu.

Appendix A: Supplementary Material

Additional figures for representative fits and uncertainty analyses for each sample may be found in the Supplementary Materials.

REFERENCES

[1] A. S. Brouwer, M. van den Broek, A. Seebregts, and A. Faaij, "Operational flexibility and economics of power plants in future low-carbon power systems," Applied Energy **156**, 107–128 (2015).

[2] N. L. Brun and C. N. Markides, "A galinstan-filled capillary probe for thermal conductivity measurements and its application to molten eutectic kno3–nano3–no2 (hts) up to 700 k," International Journal of Thermophysics **36**, 3222–3238 (2015).

[3] T. Delise, A. C. Tizzoni, M. Ferrara, N. Corsaro, C. D'Ottavi, S. Sau, and S. Licoccia, "Thermophysical, environmental, and compatibility properties of nitrate and nitrite containing molten salts for medium temperature csp applications: A critical review," Journal of the European Ceramic Society **39**, 92–99 (2019).

[4] P. Sabharwall, M. Ebner, M. Sohal, P. Sharpe, M. Anderson, K. Sridharan, J. Ambrosek, L. Olson, and P. Brooks, "Molten salts for high temperature reactors: University of wisconsin molten salt corrosion and flow loop experiments-issues identified and path forward," (2010).

[5] C. Fiorina, A. Cammi, L. Luzzi, K. Mikityuk, H. Ninokata, and M. E. Ricotti, "Thermal-hydraulics of internally heated molten salts and application to the molten salt fast reactor," (Institute of Physics Publishing, 2014).

[6] A. I. Elshafei, A. Guaily, and M. A. Boraey, "Comparative study of nusselt number correlations for hitec molten salt," (Institute of Electrical and Electronics Engineers Inc., 2020) pp. 282–287.

[7] J. Magnusson, M. Memmott, and T. Munro, "Review of thermophysical property methods applied to fueled and un-fueled molten salts," Annals of Nuclear Energy **146** (2020), 10.1016/j.anucene.2020.107608.

[8] S. Guillot, A. Faik, A. Rakhmatullin, J. Lambert, E. Veron, P. Echegut, C. Bessada, N. Calvet, and X. Py, "Corrosion effects between molten salts and thermal storage material for concentrated solar power plants," Applied Energy **94**, 174–181 (2012).

[9] E. R. V. Artsdalen, I. S. Y. Vol, B. E. R. V. Artsdalen, I. S. Yaffe, H. Bloom, J. W. Knaggs, J. J. MolIoy, D. Welch, T. F. Soc, S. V. Karpachev, A. G. Stromberg, N. Padchainova, Z. O. Khim, J. O. Edwards, C. S. Taylor, A. S. Russell, L. F. Maranville, J. E. Soc, P. W. Huber, V. Potter, H. W. S. Clair, U. S. Bureau, A. E. van Arkel, E. A. Flood, and N. F. H. Bright, "Electrical conductance and density of molten salt systems: Kcl-licl, kcl-nacl and kcl-ki," (1954).

[10] G. Gao, F. H. Stott, J. L. Dawson, and D. M. Farrell, "Electrochemical monitoring of high-temperature molten-salt corrosion," Oxidation of Metals **33**, 79–94 (1990).

[11] M. Rosenthal, R. Briggs, and P. Haubenreich, "Molten-salt reactor program," (1967).

[12] V. Khokhlov, I. Korzun, V. Dokutovich, and E. Filatov, "Heat capacity and thermal conductivity of molten ternary lithium, sodium, potassium, and zirconium fluorides mixtures," Journal of Nuclear Materials **410**, 32–38 (2011).

[13] M. Harada, A. Shioi, T. Miura, and S. Okumi, "Thermal conductivities of molten alkali metal halides," Ind. Eng. Chem. Res. **31**, 2400–2407 (1992).

[14] S. Kitade, Y. Kobayashi, Y. Nagasaka, and A. Nagashima, "Measurement of the thermal conductivity of molten kno3 and nano3 by the transient hot-wire method with ceramic-coated probes," High Temperatures - High Pressures **21**, 219–224 (1989).

[15] R. Santini, L. Tadrist, J. Pantaloni, and P. Cerisier, "Measurement of thermal conductivity of molten salts in the range 100-500°c," International Journal of Heat and Mass Transfer **27**, 623–626 (1984).

[16] C. D. Chliatzou, M. J. Assael, K. D. Antoniadis, M. L. Huber, and W. A. Wakeham, "Reference correlations for the thermal conductivity of 13 inorganic molten salts," Journal of Physical and Chemical Reference Data **47** (2018), 10.1063/1.5052343.

[17] M. C. Wingert, A. Z. Zhao, Y. Kodera, S. J. Obrey, and J. E. Garay, "Frequency-domain hot-wire sensor and 3d model for thermal conductivity measurements of reactive and corrosive materials at high temperatures," The Review of scientific instruments **91** (2020), 10.1063/1.5138915.

[18] M. Gonik and V. Golyshev, "High-temperature thermophysical properties of nonscattering semitransparent materials iii: thermal conductivity of melts," High Temperatures- High Pressures **24**, 677–688 (1992).

[19] V. Golyshev and M. Gonik, "High-temperature thermophysical properties of nonscattering semitransparent materials i: Methods and instrumentation for the determination of spectral absorptivity and thermal conductivity of melts," High Temperatures- High Pressures **24**, 367–377 (1992).

[20] P. Hartvigsen, *Raman Thermometry for Uranium Dioxide and Needle Probe for Molten Salts*, Master's thesis (2020).

[21] J. E. Daw, J. L. Rempe, and D. L. Knudson, "Hot wire needle probe for in-reactor thermal conductivity measurement," IEEE Sensors Journal **12**

(2012), 10.1109/JSEN.2012.2195307.

[22] ASTM, "D 5334-14 standard test method for determination of thermal conductivity of soil and soft rock by thermal needle probe procedure," (2011).

[23] M. Corradini, M. Anderson, G. Imel, T. Blue, J. Roberts, and K. Davis, "Advanced instrumentation for transient reactor testing," (2018).

[24] S. S. Raiman, G. Muralidharan, R. T. Mayes, and J. M. Kurley, "Compatibility studies of cladding candidates and advanced low-cr superalloys in molten nacl-mgcl 2," (2019).

[25] D. Maillet, S. Andre, J. C. Batsale, A. Degiovanni, C. Moyne, C.-I. National, P. D. Lorraine, U. Henri, I. Nancy, J. Wiley, B. Lane, W. Sussex, and P. Iud, *Thermal Quadrupoles: Solving the Heat Equation through Integral Transforms* (John Wiley Sons, Inc., 2000).

[26] C. Hollar, *Material Properties of Thermoelectric and Nuclear Energy Sources*, Ph.D. thesis (2019).

[27] C. B. Jensen, *Bridging the Nano- and Macro-Worlds: Thermal Property Measurement Using Thermal Microscopy and Photothermal Radiometry – Application to Particle-Irradiation Damage Profile in Zirconium Carbide*, Ph.D. thesis (2014).

[28] A. Salazar and R. Celorrio, "Application of the thermal quadrupole method to the propagation of thermal waves in multilayered cylinders," Journal of Applied Physics **100** (2006), 10.1063/1.2400403.

[29] C. Hollar, A. Fleming, K. Davis, R. Budwig, C. Jensen, and D. Estrada, "A parametric study for in-pile use of the thermal conductivity needle probe using a transient, multilayered analytical model," International Journal of Thermal Sciences **145** (2019), 10.1016/j.ijthermalsci.2019.106028.

[30] K. J. Hollenbeck, "Invlap.m: A matlab function for numerical inversion of laplace transforms by the de hoog algorithm," (1998).

[31] C. Xing, T. Munro, C. Jensen, and H. Ban, "Analysis of the electrothermal technique for thermal property characterization of thin fibers," Measurement Science and Technology **24** (2013), 10.1088/0957-0233/24/10/105603.

[32] M. L. Ramires, C. A. N. Castro, Y. Nagasaka, A. Nagashima, M. J. Assael, and W. A. Wakeham, "Standard reference data for the thermal conductivity of water," Journal of Physical and Chemical Reference Data **24** (1995), 10.1063/1.555963.

[33] A. Z. Zhao, M. C. Wingert, and J. E. Garay, "Frequency-domain hot-wire measurements of molten nitrate salt thermal conductivity," Journal of Chemical and Engineering Data **66** (2021), 10.1021/acs.jced.0c00621.

[34] M. L. Ramires, C. A. N. D. Castro, R. A. Perkins, Y. Nagasaka, A. Nagashima, M. J. Assael, and W. A. Wakeham, "Reference data for the thermal conductivity of saturated liquid toluene over a wide range of temperatures," Journal of Physical and Chemical Reference Data **29**, 133–139 (2000).

[35] M. J. Assael, E. A. Sykioti, M. L. Huber, and R. A. Perkins, "Reference correlation of the thermal conductivity of ethanol from the triple point to 600 k and up to 245 mpa," Journal of Physical and Chemical Reference Data **42** (2013), 10.1063/1.4797368.

[36] L. Riedel, G. M. Mallan, J. R. Woolf, W. M. Vanderkooi, and Y. Rastorguev, "Design institute for physical properties,".

[37] K. Khoshmanesh, S. Y. Tang, J. Y. Zhu, S. Schaefer, A. Mitchell, K. Kalantar-Zadeh, and M. D. Dickey, "Liquid metal enabled microfluidics," Lab on a Chip **17**, 974–993 (2017).

[38] S. Yu and M. Kaviany, "Electrical, thermal, and species transport properties of liquid eutectic ga-in and ga-in-sn from first principles," Journal of Chemical Physics **140** (2014), 10.1063/1.4865105.